Journal of Biology and Today's World
Journal home page: http://journals.lexispublisher.com/jbtw

Received: 22 June 2016 • Accepted: 28 August 2016

Review

doi:10.15412/J.JBTW.01050802

The Kirkendall Effect: its Efficacy in the Formation of Hollow Nanostructures

Rezvan Dehdari Vais, Hossein Heli*

Nanomedicine and Nanobiology Research Center, Shiraz University of Medical Sciences, Shiraz, Iran

*Correspondence should be addressed to Hossein Heli, Nanomedicine and Nanobiology Research Center, Shiraz University of Medical Sciences, Shiraz, Iran; Tel: +987136282225; Fax: +987136281506; Email: heli7@yahoo.com; heli@sums.ac.ir.

ABSTRACT

The Kirkendall effect refers to the formation of the so-called 'Kirkendall voids' caused by the difference in diffusion rates between two species. It is a classical phenomenon in metallurgy and since its discovery, the Kirkendall effect has been observed in different alloy systems. The development of the hollow interior consists of two main steps. The first step is the formation of the small Kirkendall voids near the original interface via a bulk diffusion process. The second step is a consequence of the surface diffusion of the core material (the fast-diffusing species) along the pore surface. Since hollow and porous structures have attracted tremendous attention due to their common applications in sensor systems, chemical reactors, catalysis, drug delivery, environmental engineering, biotechnology, etc., the Kirkendall effect dominates in the fabrication of hollow nanostructures. These nanostructures play a key role in the biological applications of hollow materials such as labeling of cellular structures/molecules, drug loading, encapsulation, delivery and release, bio-labeling, biosensors, magnetic resonance imaging, and biomedicine vehicles.

Key words: Kirkendall Effect, Hollow Structures, Nanostructure Synthesis.

Journal of Biology and Today's World is published by *Lexis Publisher*; Journal p-ISSN 2476-5376; Journal e-ISSN 2322-3308.

1. INTRODUCTION

Ernest Kirkendall investigated the inter-diffusion between copper and zinc in brass at high temperatures (1, 2). He observed a shift in the initial interface and shrinkage in the core of the brass alloy due to unequal diffusion rates of copper and zinc atoms in brass. This is shown in Figure 1 (2, 3). In this figure, the dash square indicates the interface between β-brass and copper at the start of the experiment (the diffusion interface). The square with the length D is the original β-brass and copper interface. The width B represents a shell of α-brass which is newly formed. The internal square indicates the exterior boundary of β-brass at time t. The space A represents the real volume change of α-brass. In fact, β-brass changes to a denser copper-α-brass due to the transition of the original interface. From the results of this experiment, Kirkendall concluded that zinc diffusion into copper is faster than the copper diffusion into the brass (2, 4). Whereas, the essential diffusivity of zinc was ≈2.5 times of copper at elevated temperature. This process led to the real displacement of the initial interface. Also, the Kirkendall experiment proved that the defect formation is a consequence of different diffusivities of the lattice atoms. These atomic defects are the so-called vacancies in most alloys and metals. Accumulation of additional vacancies can result in the formation of 'Kirkendall voids' near the bond interface. This phenomenon is known as the Kirkendall effect. The formation of the Kirkendall voids affects the properties of the interfaces and weakens the bonding strength of the interface. Basically, the Kirkendall voids are considered as a troublemaker (2, 5). However, in recent years, the Kirkendall effect has been applied in nanotechnology for the design and fabrication of hollow structures (6). When the inter-diffusion between two parts of a nanomaterial is unequal, the net rate of vacancy production leads to the formation of a single void, finally resulting in the formation of hollow structures. Synthesis of nanostructured materials with hollow interiors is particularly important due to potential applications of these materials in chemical reactors, sensor systems, catalysis, drug delivery, ion exchange, encapsulation, environmental engineering, energy-storage media, biomedical diagnosis, artificial cells, and the paint industry (4, 7-12). Therefore, the Kirkendall effect, as one of the effective diffusion methods, has recently attracted the interest of many researchers for the synthesis and study of hollow

nanostructures (3, 6, 7). It is worth mentioning that there are some synthetic strategies such as hard templating, sacrificial templating, soft templating and template-free methods for the synthesis of hollow structures, wherein the Kirkendall effect could play a vital role, such as synthesis of diverse hollow nanostructures of chalcogenides, phosphides, sulfides, selenides and metal-oxides (4).

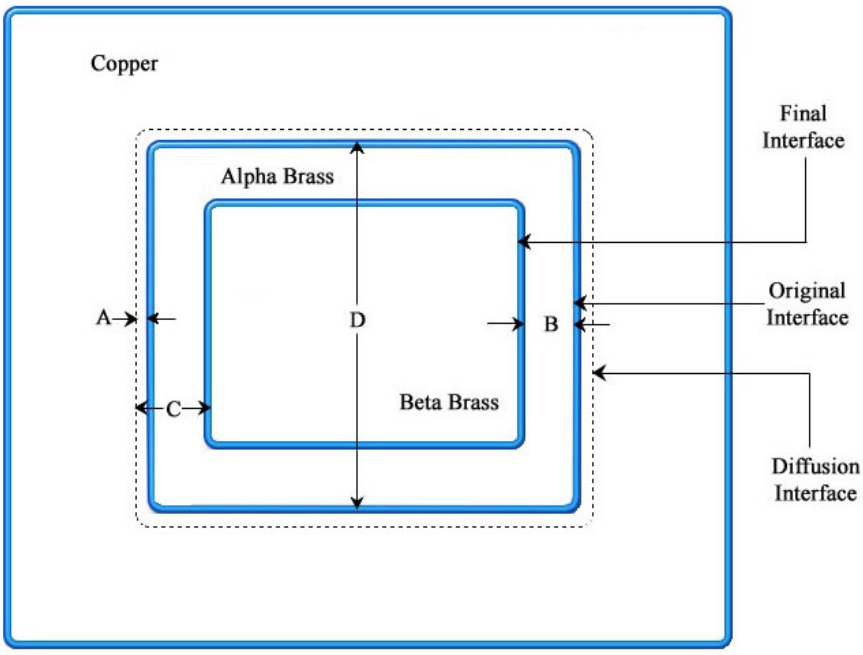

Figure 1. A conventional model for the Kirkendall effect and evaluation of the inter-diffusion of copper and zinc in brass

Therefore, different hollow nanostructures can be synthesized under domination of the Kirkendall effect. These hollow nanostructures have a higher surface to volume ratio, compared to the solid counterparts with the same sizes. Various drugs and biomolecules can be incorporated in the interior part of the hollow nanostructures, while their outer surfaces can be functionalized by active or targeting agents (13, 14). Hollow nanostructures have applications in different areas of biomedicine including simultaneous diagnosis and therapy (15). In 2004, Alivisatos and co-workers utilized the Kirkendall effect for the first time in formation of hollow spherical cobalt sulfide nanocrystals. In the synthesis process, cobalt nanocrystals reacted with elemental sulfur at ≈180 °C. A consequence of this reaction was transformation of metallic cobalt nanocrystals into hollow cobalt sulfide nanocrystals of either Co_3S_4 or Co_9S_8, depending on the sulfur-to-cobalt molar ratio used in the synthesis. The formation of hollow cobalt sulfide nanocrystals was attributed to the outer-diffusion of cobalt atoms being faster than that of the inter-diffusion of sulfur atoms (4, 16). In this paper, after a brief presentation of the theory of the Kirkendall effect, formation of different types of nanostructures via this physical phenomenon was reviewed.

2. THEORY

Substitutional diffusion, as a kinetic phenomenon, has a vital role in solid-state phase transformations (17). The kinetics of the Kirkendall-type diffusion is explained based on a common model of one-dimensional steady-state diffusion controlled by Fick's first law (diffusion of mass and the vacancies by concentration gradient) (5, 18). Figure 2 shows the interface of two materials A and B, which can inter-diffuse together with unequal diffusion rates.

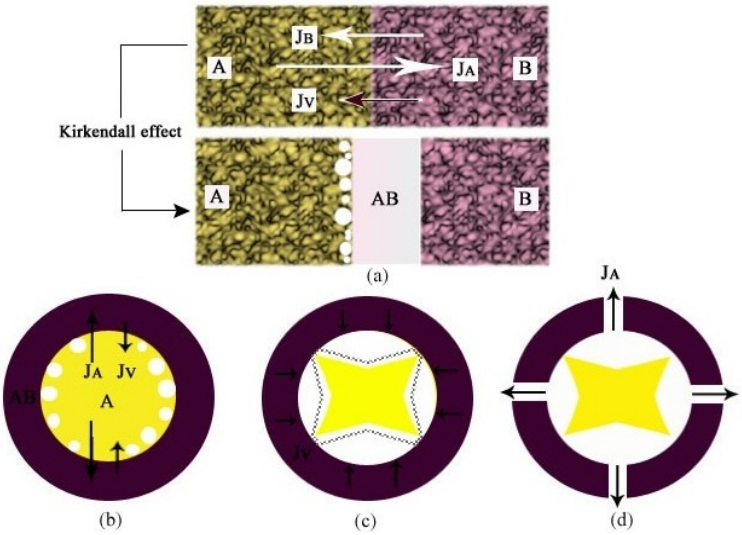

Figure 2. Schematic illustration of an unequal diffusion fluxes at the interface of two materials A and B (a). The unequal of atomic fluxes are equilibrated by means of a flux of vacancies. A stepwise mechanism for the generation of hollow nanostructures via the Kirkendall effect (b-d). The formation of voids near the interface via bulk diffusion (b). The expansion of the hollow core by the surface diffusion process (c). The material exchange proceeds through the revealed gaps during the growth that this gap resulted in the evacuation of the nanoparticles (d)

In Figure 2 (a), for the diffusion fluxes if $J_A > J_B$, the voids are formed close to the A/AB interface during the bulk inter-diffusion of vacancies. Therefore, a net flux of vacancies is generated that equilibrates the unequal atomic fluxes ($J_v = J_A - J_B$). These voids are in contact with the inner product surface, and then the hollow core is propagated by the surface diffusion of the remaining A atoms. The material exchange continues via direct dissolution in solution phase or evaporation in gas phase, and the gaps lead to emptying the particles (Figure 2 (d)). The kinetics of the volume flux and also inspected timescales and the experimental standard for the fabrication of hollow nanospheres were discussed (2, 5). These treatments were investigated using a spherically layered structure of $Ni/Ni_2Si/Si$, as an example. Assume a spherical particle of nickel as the core, and another spherical particle of silicon as the shell. Reaction of the core and shell generates the compound Ni_mSi_n which shapes up between nickel and silicon. If r_1 and r_2 are the radius of the inner and outer surface of Ni_mSi_n, respectively, the outward growth rate of Ni_mSi_n layer at time t will be:

$$dr_2 / dt = \{[n_{Ni} D_{Ni} \Delta C_{Ni} r_1]\} / [r_2 (r_2 - r_1)] \quad (1)$$

where n_{Ni} is the volume density of nickel in the Ni_mSi_n layer and D_{Ni} and ΔC_{Ni} are the diffusivity and concentration difference, respectively. To generate the hollow structures, the following condition must be attained:

$$\{n D_{Ni} |\Delta C_{Ni}| / m D_{Si} |\Delta C_{Si}|\} + 1 > r_2^3 - r_1^3 \quad (2)$$

Figure 3 (a) shows a bilayer structure of Ni/Si; a Ni_2Si layer is formed at the Ni/Si interface after annealing. In this structure, the nickel diffusivity is greater than that of silicon for the growth of Ni_2Si. It is obvious that the interfacial area doesn't change during the growth, and the thickening of the layered structure occurs. The layer thickening is controlled by Fick's first law of diffusion. The velocity of the interface between Ni_2Si and silicon is:

$$dx_{\beta\gamma} / dt = [D_\beta / C_{\beta\gamma}^{eq} - C_{\gamma\beta}^{eq}] [dC_\beta / dx] \quad (3)$$

D_β denotes the diffusion coefficient of nickel in Ni_2Si, dC_β / dx represents the concentration gradient of nickel at the Ni_2Si/Si interface, $C_{\beta\gamma}^{eq}$ and $C_{\gamma\beta}^{eq}$ indicate equilibrium concentrations of nickel in Ni_2Si and silicon, and $dx_{\beta\gamma} / dt$ denotes the velocity of the interface between Ni_2Si and silicon. There is a parabolic dependence of layer thickness on time in diffusion-governed process. In Figure 3 (b), the outer-diffusion of nickel to create a shell of Ni_2Si will result in a void in the core of nanostructure. Considering that, the thickening of a shell of Ni_2Si transforms both the interface areas. The effect of the Gibbs-Thomson potential has been examined in the thickening rate of the compound layer (the diffusion phenomenon thermodynamically materialized due to the difference of the chemical potential of atoms between the inner and outer surfaces in nanospheres). Here, the focus is on the outer-diffusion of nickel species and the enlargement rate of the spherical interface at r_2 is (18):

$$dr_2 / dt \approx (D_\beta / kT) [-\Delta\mu_\beta / (r_2 - r_1)] \quad (4)$$

where

$$\Delta\mu_\beta = \Delta G_{silicide} + (2\gamma_2\Omega/r_2 + 2\gamma_1\Omega/r_1) = \Delta G_{silicide} + 2\Omega (\gamma_2/r_2 + \gamma_1/r_1) \quad (5)$$

In the above equation, r_1 and r_2 are the position of the inner and outer boundaries, respectively, Ω is the atomic volume of nickel in the product phase, $\Delta G_{silicide}$ represents the formation energy of Ni_2Si phase, and γ_1 and γ_2 denote the interfacial energy. Equation (1) refers to the direction reaction that is governed by thermodynamics. In the cases whose quantities of r_1 and r_2 are very small, and the interfacial energy (γ) is very high, the Gibbs-Thomson effect may thermodynamically prevent the outer-diffusion flux in equation (1). Consequently, the hollow nanostructures can't be formed by an external pressure. This process can be explained by the equation: $\sigma = 2\gamma/r$, and the applied stress σ leads to a shrinkage in the pore size since the extra vacancy accumulation is reduced. The vacancy concentration at the inner surface which is under a

negative pressure $C_V^{in} = C_V^0 \exp(2\gamma\Omega/kTr_{in})$ is greater than that of the outer surface which is under a positive pressure $C_V^{out} = C_V^0 \exp(2\gamma\Omega/kTr_{out})$ (2). Therefore, after annealing a hollow nanocrystal at high temperature, vacancy fluxes outside the inner surface are absorbed at the outer surface, and change the hollow nanocrystal to a solid nanocrystal, because the surface energy of a solid nanosphere is lower toward the surface energy of a hollow nanostructure. As a result, a hollow nanoparticle is thermodynamically unstable (18, 19).

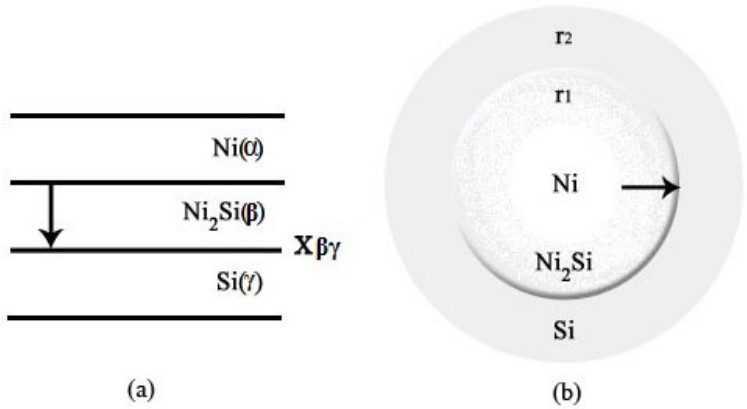

Figure 3. Schematic representation of the cross-section (a) and spherically (b) layered structures of Ni/Ni_2Si/Si. Nickel is the out-diffusing species. A Ni_2Si layer is formed at the Ni/Si interface that will result in the formation of a void in the core

Therefore, the suitable temperature is highly important. In the mentioned planner structure, a shell of Ni_2Si of nanothickness is also unstable, as shown in Figure 3 a, because it transforms into a spherical structure. It should be mentioned that in classical metallurgy, a lamellar pearlite will change into a spherical pearlite when it undergoes ageing (18).

3. HOLLOW NANOSTRUCTURES VIA THE KIRKENDALL EFFECT

3.1. Hollow nanoparticles

Hollow nanoparticles with interior void and controlled shell thickness are suitable for fabrication of lightweight materials and for catalysis and nanoelectronics applications (19, 20). In this manner, synthesis of hollow nanoparticles has attracted much attention in recent years and various methods for their preparation have been reported (21). A more conventional method to fabricate hollow nanoparticles is based on two steps. Nanoparticles are fabricated first and then the Kirkendall effect leads to formation of the hollow nanostructure. Monodispersed Fe_3O_4 hollow nanoparticles were synthesized by oxidation of Fe-Fe_3O_4 nanoparticles. Nanoparticles of Fe_3O_4, as a superparamagnetic material, were fabricated with a size smaller than 20 nm (22). Iron nanoparticles were firstly synthesized by means of thermal decomposition of iron pentacarbonil [$Fe(CO)_5$] in the presence of oleylamine (20, 22). It should be mentioned that the iron nanoparticles are chemically unstable (20). Therefore, these nanoparticles were further oxidized by air at room temperature to form the core-shell Fe/Fe_3O_4 nanoparticles. Then, the oxidation of Fe-Fe_3O_4 nanoparticles was followed up by trimethylamine N-oxide (Me_3NO) as an oxygen-transfer reagent, resulting in the formation of monodispersed hollow Fe_3O_4 nanoparticle with controlled size through the Kirkendall effect (Figure 4) (16, 21, 23). The experimental results demonstrated that adjusting the reaction temperature and time is essential (increase in the temperature >200 °C and time) to attain the conditions of formation of hollow structures through the Kirkendall effect (4). The outer-diffusion of metallic iron was faster than that of the inter-diffusion of oxygen. Thus, Fe_3O_4 accumulated at the metal-oxide interface rather than in the inner part of the core. The transmission electron microscopy (TEM) images show that the formed iron bridges between the core and shell lead to a fast outward diffusion of iron atoms and it stays joined to the shell to the extent that the core is perfectly consumed (20, 22). A similar approach dominates the synthesis of bismuth oxide hollow nanoparticles (23), hollow CoO nanoparticles (24), CuO hollow nanoparticles (25, 26) and Cu_2O hollow structure (27). Laser light was also used for oxidation and conversion of metal nanoparticles into metal oxides and sulfides (28).

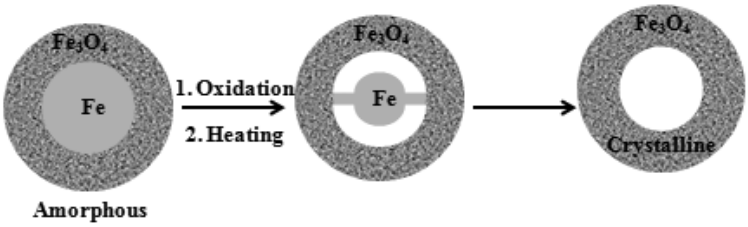

Figure 4. A stepwise mechanism for the generation of the hollow Fe_3O_4 nanoparticle

$NiFe_2O_4$ hollow magnetic nanoparticles were synthesized by $Ni_{33}Fe_{67}$ nanoparticles as the starting material via invert gas condensation technique (29). Invert gas condensation technique is the physical adsorption of a famous probe at diverse concentrations by a solid surface (30). Then, a $NiFe_2O_4$ shell was formed via the oxygen passivation of the alloy nanoparticle. Finally, the as-prepared core/shell $Ni_{33}Fe_{67}/NiFe_2O_4$ structure was annealed in the air at three temperatures of 350, 450, and 550 °C (29). During the reaction, control of the reaction temperature and time affects the final product (31). Therefore, these gas-solid reactions under optimized reaction time and temperature conditions resulted in formation and collapsing voids in the single phase $NiFe_2O_4$ structure. Figure 5 schematically illustrates the fabrication/collapse mechanism of $NiFe_2O_4$ hollow spheres. It also reveals that generation/collapse processes of $NiFe_2O_4$ hollow nanospheres are dependent on reaction temperature and time. As shown in this figure, formation of $NiFe_2O_4$ hollow structure leads to a larger surface area, compared to the non-hollow nanoparticles. Increase in the reaction temperature was a reason for a complete collapse of the holes and finally resulted in formation of non-hollow nanoparticles (29). This methodology is also suitable for fabricating other types of hollow or core-shell-void transition-metal oxide nanoparticles (20).

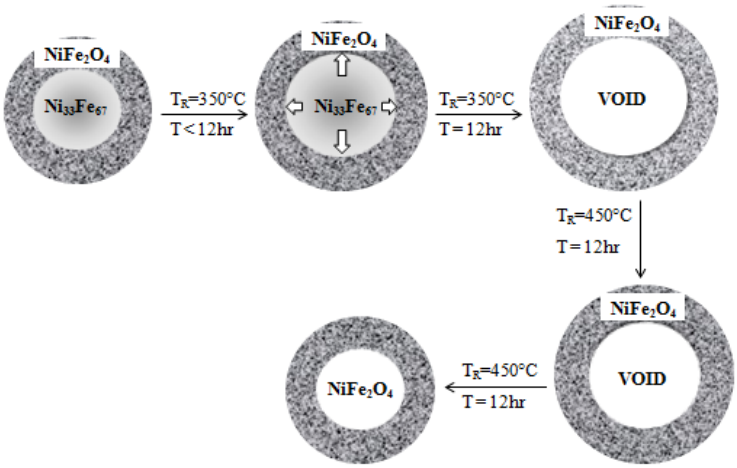

Figure 5. A schematic illustration of the fabrication/collapse mechanism of $NiFe_2O_4$ hollow spheres as a function of the reaction temperature and time

Hollow nickel oxide, sulfide, selenide, or phosphide nanoparticles (7, 32, 33) and Cu_7S_4 hollow hexagonal-like nanoparticles [34] were synthesized via the Kirkendall effect. Hollow Ni_2P Nanoparticles were synthesized using trioctylphosphine (TOP) as a phosphorus source in the solution phase at moderate temperatures. The experimental results have demonstrated that TOP, as a strong ligand toward metals, has a high reactivity with nanosized Ni particles. Thus, the first well-dispersed FCC Ni nanoparticles with an average size of about 12 nm were formed. TOP concentration has an essential role in formation of hollow products. Also, TOP can dissolve some surface atoms of Ni Nanoparticles and create Ni-TOP complexes and the compact Ni_2P Nanoparticles have probably been fabricated from decomposition of these complexes. Finally, the hollow Ni_2P Nanoparticles were formed by means of diluted TOP with a solvent such as 1-octadecene and oleylamine which was also used as a protecting surfactant for the same reaction. According to the Kirkendall effect, at sufficiently high temperature the diffusion of Ni in the core crossing the prior formed Ni_2P layer is faster than that of phosphorus atoms. The void was formed at the center due to the net inward flux of vacancies. These hollow nanoparticles are a single crystal (7). This approach was also applied to the synthesis of hollow intermetallic Ni-Zn nanoparticles (34, 35). In Table 1,

hollow nanoparticles synthesized via the Kirkendall effect were summarized.

Table 1. Hollow nanoparticles synthesized via the Kirkendall effect

Material	Synthesis route	Reference
Ni_2O hollow nanoparticles	Reaction of nickel acetate, oleylamine, trioctylphosphine and 1-octadecene	(7)
Monodispersed Fe_3O_4 hollow nanoparticles	Oxidation of Fe-Fe_3O_4 nanoparticles	(22)
Bismuth oxide hollow nanoparticles	Thermal decomposition of bismuth 2-ethylhexanoate dissolved in a mixture of oleylamine and dichlorobenzene	(23)
Hollow CoO nanoparticles	Chemical transformation of cobalt nanoparticles through oxidation in air	(24)
CuO hollow nanoparticles	Oxidizing copper/graphene at 300 °C	(25)
CuO hollow nanospheres	Thermal oxidation with Cu_2O solid nanospheres	(26)
Cu_2O hollow structure	Oxidation of copper nanoparticles	(27)
ZnS hollow nanoparticles	Oxidation and conversion of metal nanoparticles by laser light	(28)
$NiFe_2O_4$ hollow nanoparticles	Invert gas condensation using $Ni_{33}Fe_{67}$ nanoparticles	(29)
Ni_2P hollow nanoparticles	Mild temperature solution reaction using triphenylphosphine	(32)
Ni_2P hollow nanoparticles	Reaction of metal nanoparticles with a phophorus precursor	(33)
NiS hollow nanoparticles	Reaction of metal nanoparticles with a sulfide precursor	(33)
NiSe hollow nanoparticles	Reaction of metal nanoparticles with a selenide precursor	(33)
Cu_7S_4 hollow nanoparticles	Template-based method using Cu_2O nanocubes	(34)
Ni-Zn hollow nanoparticles	Chemical conversion of nickel nanoparticles	(35)
Hollow cobalt oxide nanoparticles	Deposition on a water-air interface	(36)
Pt-based hollow nanoparticles	Electrosynthesis	(37)
CdSe hollow nanoparticles	Slow heating of a low-melting-point metal salt	(38)
Porous hollow iron oxide nanoparticles supported on CNTs[a]	Fe@Fe_xO_y/CNT etching with dilute nitric acid	(39)
Single crystal hollow silver nanoparticles	Reduction of silver oxide nanoparticles capped with glutathione	(40)
α-Fe_2O_3 hollow nanoparticles	Oxidation of carbon-encapsulated iron carbide nanoparticles in air	(41)
Fe_3O_4 hollow nanospheres	Iron nanoparticles oxidation	(42)
$Mg(NH_2)_2$ hollow nanospheres	NH_3 reaction with Mg_3N_2 nanocubes	(43)

[a]Carbon nanotubes

3.2. Hollow nanotubes

Spinel oxides with the composition of AB_2O_4 are generated according to the following reaction:

$$AO + B_2O_3 \rightarrow AB_2O_4 \qquad (6)$$

where A and B are metals with the valences of (II) and (III), respectively (44). Metal aluminates (MAl_2O_4) with spinel structure have attracted much attention because of their technological applications such as oxidation catalysts, pigment and high alumina cement. Also, nanostructured aluminates achieve improved properties like better diffusion, greater thermal stability, and ductility (45). Hollow single-crystal $ZnAl_2O_4$ spinel nanotube was synthesized (16). Firstly, single-crystalline ZnO nanowires (Figure 6 a), as substrate, were synthesized via the vapor phase method. Then, the nanowires were uniformly coated with Al_2O_3 by atomic layer deposition (ALD) and the thickness of the Al_2O_3 wall was governed by means of the number of ALD cycles (16, 46, 47). The precipitation occurred at 200 °C by means of trimethylaluminum [$Al(CH_3)_3$] and water as the alumina and oxygen precursor (2, 16). Therefore, a core-shell nanowire (ZnO-Al_2O_3, Figure 6 b) is the starting material. The core/shell nanowires were annealed into an open quartz tube oven at 700 °C for 3h, resulting in the interfacial solid-state reaction and preferential outwarding the ZnO species. The voids are generated near the interface and final $ZnAl_2O_4$ spinel nanotubes with a wall thickness of ~10 nm and a diameter of ~40 nm were obtained (Figure 6 c). If a dendritic ZnO nanocrystal is used as the substrate, the same annealing and ALD process, the branched tubular spinel nanocrystals will be obtained (16). An important point in this process is the reaction temperature during the

annealing process, because a reasonable temperature caused the formation of spinel nanotubes with a governed wall thickness (48).

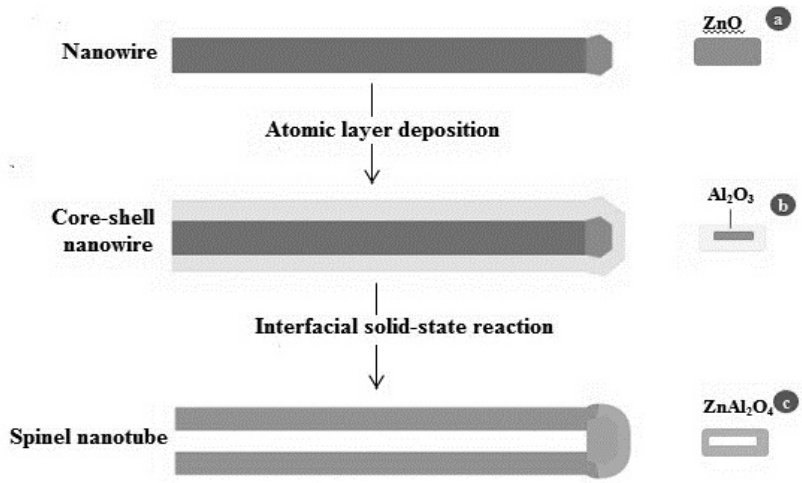

Figure 6. Schematic representation of the formation mechanism of the $ZnAl_2O_4$ spinel nanotubes

For the synthesis of $MgAl_2O_4$, MgO nanowires were employed. MgO nanowires are highly reactive, and then they act as a sacrificing template for $MgAl_2O_4$. Also, spinels such as $MgAl_2O_4$, $MgFe_2O_4$, $MgIn_2O_4$, $MgCr_2O_4$ can be synthesized by reactions between the MgO substrate and the other oxide (49). Figure 7 shows the reaction steps of the samples synthesized with this route. Again, the outer-diffusion of ZnO core in the spinel layer is greater than the inter-diffusion of the Al_2O_3 shell.

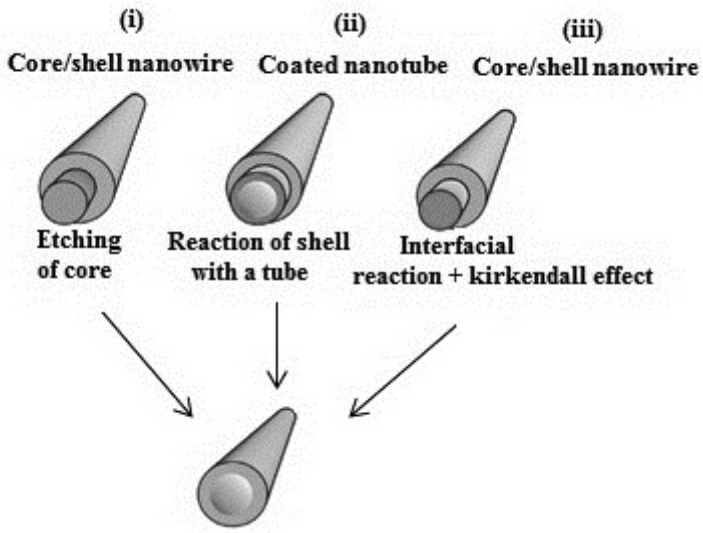

(a)

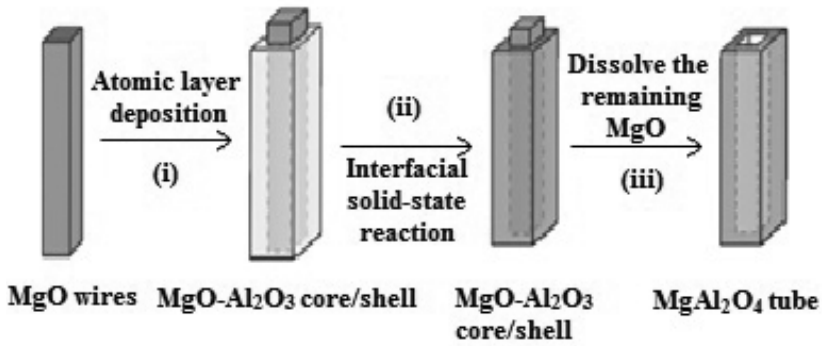

(b)

Figure 7. Formation of nanotubes using nanowire or nanotube templates. Fabrication of core-shell nanowires by means of elimination of the core via etching or dissolution (a). Formation of complex compositions by reaction between shell material and a tube (b)

ZnO-ZnS core-shell nanowires were synthesized by sulfidation of ZnO nanowires through the Kirkendall effect (50). The Kirkendall effect caused the formation of hexagonal-shape voids inside the crystalline ZnO core and six symmetrically located {1010} planes. In another study, polycrystalline Co_9S_8 nanotubes were synthesized using $Co(CO_3)_{0.35}C_{l0.20}(OH)_{1.10}$ nanorod bunches as sacrificial hard templates through a hydrothermal route (51). Co_9S_8 nanotubes were formed due to the difference in diffusion rates between the cobalt source and the sulfur ions. These nanotubes show paramagnetic property instead of ferromagnetic property, which may be due to the fact that the nanotubes are composed of many tiny nanoparticles. In Table 2, hollow nanotubes synthesized via the Kirkendall effect are summarized.

Table 2. Hollow nanotubes synthesized via the Kirkendall effect

Material	Synthesis route	Reference
$ZnAl_2O_4$ hollow nanotubes	Template-based method using ZnO nanowires	(16)
$MgAl_2O_4$ hollow nanotubes	Template-based method by reactions between the MgO substrate and the other oxide	(49)
$MgFe_2O_4$ hollow nanotubes	Template-based method by reactions between the MgO substrate and the other oxide	(49)
$MgIn_2O_4$ hollow nanotubes	Template-based method by reactions between the MgO substrate and the other oxide	(49)
$MgCr_2O_4$ hollow nanotubes	Template-based method by reactions between the MgO substrate and the other oxide	(49)
ZnO-ZnS core-shell nanowires	Sulfidation of ZnO nanowires	(50)
Co_9S_8 nanotubes	Hydrothermal reaction	(51)
SnO_2 nanofibers/nanotubes	Electrospinning method	(52)
Carbon-SnO_2 core-shell hybrid nanofibers	Electrospinning method	(53)
ZnO nanotubes	Hydrothermal reaction	(54)
Thin tubular ZnO nanostructure	Hydrothermal reaction	(55)
Zn_2SnO_4 nanotubes	Hydrothermal reaction	(56)
Zr-doped ceria nanotubes	Hydrothermal reaction	(57)
ZnO-carbon composite tubular	Hydrothermal reaction	(58)
$SrTiO_3$ nanotubes	Hydrothermal reaction	(59)
Co_3S_4 nanotubes	Hydrothermal reaction	(60)
Tubular $BaTiO_3$	Solvothermal method	(61)
Manganese ferrite nanotubes	Solvothermal method	(62)
Co_3O_4 nanotubes	Oxidation process	(63)
NiO nanotubes	Oxidation process	(64)
Ultra-thin ZnO nanotubes	Oxidation process	(65)
Co_3O_4, ZnS, CdS, and CdSe nanotubes	Oxidation process	(66)
Cu_2O and CuO nanotubes	Thermal oxidation method	(67)
Nickel oxide nanotubes	Thermal oxidation method	(68)
Sn doped CuO nanotubes	Thermal oxidation method	(69)
Crystalline Bi_2Te_3 nanotubes	Solution-based method	(70)
ZnS nanotubes	Solution-based method	(71)
Single-crystal ZnO nanorods	Solution-based method	(71)
Ferric molybdate nanotubes	Solid-state reaction	(72)
Ferric molybdate nanotubes	Solid-state reaction	(73)
MgO nanotube	Gas-solid reaction	(74)
CuS nanotube	Gas-solid reaction	(75)
CeO_2 Nanotubes	Solid-liquid reaction	(76)
ZnS on ZnO nanorods	Sulfidation method	(77)
$Ni_{0.5}Zn_{0.5}Fe_2O_4$ nanowire-in nanotubes	Electrospinning method	(78)
$NiCo_2S_4$ porous nanotubes	Template-based method	(79)
Ni_2P nanotubes	Template-based method	(80)
Cu-Au alloy nanotubes	Template-based method	(81)
Cu_2O Nanotubes	Template-based method	(82)
ZnO nanotubes	Template-based method	(83)
ZnO nanoflakes	Template-based method	(83)
Silver-doped CeO_2 nanotubes	Deposition-based method	(84)
Coaxial microtuble nanolaminate	Atomic layer deposition	(85)
$Cr_2Te_4O_{11}$ and Mn_2TeO_6 nanotubes	Chemical conversion method	(86)
ZnO/ZnS core/shell nanorods and diverse metal sulfide nanotubes	Chemical conversion method	(87)
FeS nanotubes	Sulfurization	(88)
poly(o-toluidine) nanofibers and nanotubes	Swelling-evaporation method	(89)
Zn_2SiO_4-SiO_x coaxial nanotubes	One-step thermal annealing process	(90)
Zn_2SiO_4-nanoparticle-chain-embedded SiO_x nanotubes	One-step thermal annealing process	(90)
Zn_2SiO_4-SiO_x coaxial nanotubes	One-step thermal annealing process	(90)
$Fe(OH)_3$ nanotubes	Calcination	(91)
$CdCl_2$ nanotubes	Head-to-end assembled process	(92)
Platinum nanotubes	Sacrificing the exterior of tellurium nanowires	(93)
$NaNbO_3$ nanotubes	A multi-step reaction	(94)
Copper oxide nanotubes	Magnetron sputtering deposition-thermal oxidation	(95)
Cadmium nanocrystalline shells	Chemical reactions	(96)
Platinum nanotubes with single crystalline nanoflakes	Sacrificing the nickel nanorods	(97)

3.3. Hollow nanoneedles

Inorganic hollow needle-shaped nanostructures have attracted much attention due to their applications in field-emitting devices, novel optoelectronic, and biosensors. Furthermore, nanoneedles with hollow interior represent a lower density and higher surface area toward solid nanoneedles (36, 98, 99). ZnS hollow nanoneedles were synthesized based on Kirkendall effect (36, 98). In the synthesis, ZnO nanoneedles with lower symmetrical geometries were used as self-sacrificed templates. ZnO nanoneedles show a high rate of electron tunneling and high electric field (36). These nanoneedles have a sharp tip with a radius of about 8.9 nm which would make electron emission easy (100). Therefore, they represent a powerful ultraviolet excitonic emission but slight visible emission.

These nanoneedles can be synthesized via various approaches such as vapor phase method on silicon or gallium-doped ZnO film substrate (36, 101). Thioacetamide (TAA) was also used as a sulfide source for the synthesis of ZnS hollow nanoneedles. The reactions are:

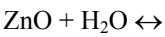

$ZnO + H_2O \leftrightarrow Zn^{2+} + 2OH^-$ (7)

$CH_3CSNH_2 + 3OH^- \leftrightarrow CH_3COO^- + NH_3 + S^{2-} + H_2O$ (8)

$CH_3CSNH_2 + H_2O \leftrightarrow CH_3CONH_2 + H_2S$ (9)

$H_2S \leftrightarrow HS^- + H^+$ (10)

$HS^- \leftrightarrow S^{2-} + H^+$ (11)

$S^{2-} + Zn^{2+} \rightarrow ZnS$ (12)

Sulfide ions were released from TAA and react with dissolved zinc ions from ZnO needles at 90-120 °C for 5h (Figure 8 a1).

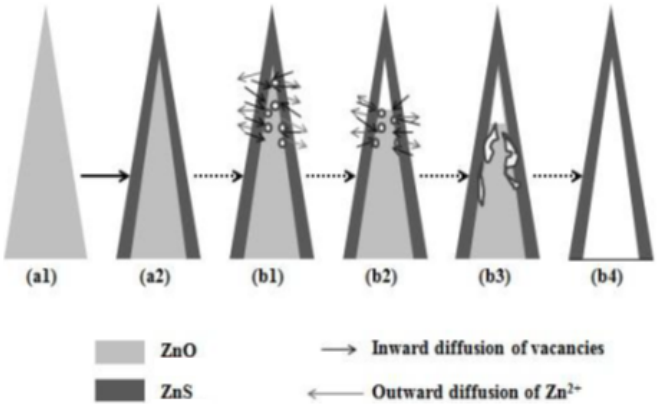

Figure 8. A schematic image of the fabrication of ZnS hollow nanoneedles based on the modified Kirkendall effect

As a result, the ZnS shell shapes up on the ZnO surface (ZnO/ZnS) via chemical reaction (Figure 8 a2). Simultaneously, the reaction between TAA and hydroxyl ions initiates an excessive driving force for the Zn outer-diffusion from the ZnO needle core and finally the Kirkendall effect will lead to formation of ZnS hollow nanoneedles at 120°C (Figure 8 a). The zinc outer-diffusion from ZnO needle core leads to formation of vacancies at the interface of the ZnO core and the ZnS shell (Figure 8 b1). Then the extra vacancies can form the void at the tip (Figure 8 b2). The bottom part of the nanoneedle has a bigger size as compared to the tip; for this reason, diffusion is very hard. It should be mentioned that the multiple voids formed in this part and at the end part (Figure 8 b3) resulted in formation of the core and shell. Consequently, the multiple voids accumulate into a single void after migration due to the decrease in the surface energy. The tip part has also a small size; therefore, the formed voids can be sealed. However, the sealing effect does not occur at the bottom end due to its large size. Therefore, ZnS hollow nanoneedles with a closed tip and an open end are generated (Figure 8 b4) (36).

3.4. Hollow nanofibers

Nanofibers are suitable candidates for a broad range of applications including high efficiency filters, drug carriers, tissue engineering and sensing (102-104). Recently, it has been demonstrated that polymer nanofibers with hollow structures can reinforce material properties for the aforementioned applications. Porous hollow SnO_2 nanofibers were synthesized based on Kirkendall effect. During this process, core/shell polyvinylpyrrolidone (PVP)/Sn precursor structures were prepared firstly by means of adding $SnCl_4.5H_2O$ into PVP dissolved in ethanol/DMF (N, N-dimethylformamide) solvent mixture. Then the solution was electrospun (105). Electrospinning as a novel and efficient fabrication process is capable of producing polymer nanofibers using an electrostatically driven jet of polymer solution or polymer melt. This electrostatic processing method uses a high-voltage electric field to fabricate solid fibers from a polymer liquid (106, 107). Also, a fibrous mat was created on an aluminum foil. Finally, these electrospun fibers were calcinated at 600 °C for 3h for the creation of hollow SnO_2 nanofibers. Therefore, PVP as the sacrificial template was decomposed rapidly. The perfect decomposition of PVP resulted in some SnO_2 particles on the surface area and the immense tin precursors in the core to fabricate a concentration gradient. It is the reason for the Kirkendall effect. In essence, the interaction between tin precursor and SnO_2 was an incentive for formation of hollow nanofibers. The outer-diffusion of tin precursor atoms (core) was greater than that of the inter-diffusion of SnO_2 atoms (shell material) and this led to the formation of an empty core. The results confirmed that the surface diffusion and lattice diffusion created nanograins on the surface of SnO_2 nanofibers. Electrospinning was also used in the synthesis of alumina nanofibers (108), ceramic hollow nanofibers (109), carbon-SnO_2 hybrid nanofibers with tunable morphology, (52) and core-shell carbon-metal oxide nanofibers (53).

3.5. Hollow nanocages

Solid-solution of ceria and zirconia-containing composites

has attracted much attention because of its redox properties, releasing capacity, oxygen storage, and thermal stability. Therefore, the formation of nearly Ce-Zr-O nanocages by the Kirkendall effect is described (110, 111). In this synthesis, monodispersed ceria nanospheres were first formed as precursors by a hydrolysis process in glycol. Afterwards, zirconium (IV) was added into the glycol. The formation mechanism of the nanospheres was a two-stage growth model in which ceria nanocrystals are nucleated first in oversaturated solution and then the formed small particles (single-crystal structures) accumulate into larger particles (the secondary structures) in polar solvents like glycol, water, and ethanol. Water condensation in the reaction system is effective on the morphology of the obtained ceria (ceria nanocrystal clusters will be spherical and nearly cubic-like at low and high water concentrations, respectively). It was obvious that the secondary particles have high reactivity and diffusing rates for the fabrication of a novel hollow structure via the Kirkendall effect. Figure 9 shows the formation mechanism of the Ce-Zr-O nanocages based on Kirkendall effect. The experimental results indicated that when spherical ceria clusters were utilized as a precursor, spherical nanocages were acquired. On the other hand, near cubic nanocages were obtained when near cubic ceria precursor was used (110).

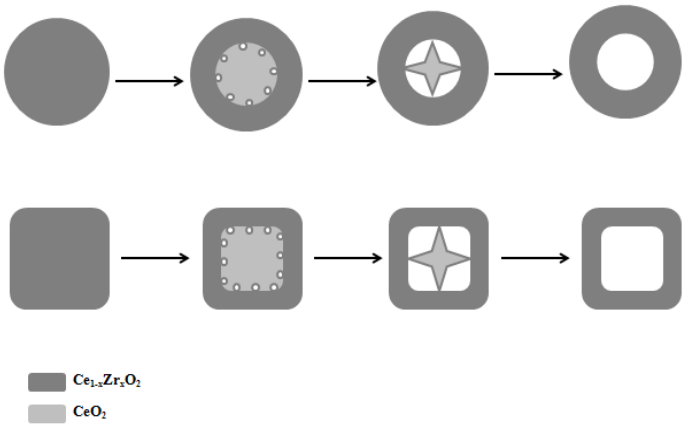

Figure 9.Schematic diagram for the generation of Ce-Zr-O nanocages via the Kirkendall effect

Sacrificial template approach based on the Kirkendall effect was applied to the synthesis of Cu_7S_4 polycrystalline nanocages (112) and Cu_2S nanocages (113). Thermal decomposition of Prussian blue analogue resulted in fabrication of Co_3O_4 porous nanocages (114) and conversion of Cu_2O nanocrystals into hollow $Cu_{2-x}Se_x$ nanocages (115) were performed by Kirkendall effect.

3.6. Yolk-shell nanostructures

Yolk-shell or rattle-typed nanostructures are recognized as a specific kind of core-shell structure with nanoparticle cores into hollow shells. In a conventional core-shell structure, the core and shell are compactly joined without any inter-space (116, 117). FePt@CoS_2 yolk-shell nanocrystals were synthesized via the Kirkendall effect. FePt@CoS_2 yolk-shell nanocrystals, as a potent agent, kill cancer cells due to their ultrahigh cytotoxity. In the synthesis process, after the generated monodispersed FePt nanoparticles via the thermal decomposition of iron pentacarbonyl ($Fe(CC)_5$) and reduction of platinum acetylacetonate (Pt $(acac)_2$), 1,2-dicholorobenzene solution of $Co_2(CO)_8$ into the refluxing solution containing oleic acid, FePt nanoparticles, and trioctylphosphine oxide, surfactant was injected for the fabrication of FePt@Co core-shell intermediates. Then a solution of sulfur dissolved in 1,2-dichlorobenzene was added to form FePt@CoS_2 yolk-shell nanocrystals via the Kirkendall effect process. The porous shells formed by the Kirkendall effect led to diffusion of Pt^{2+} ions out of the shells. Then these Pt^{2+} ions entered the nucleus and mitochondria and harmed the DNA chains. This mechanism accounts for the creation of high cytotoxicity (118). It should be mentioned that a number of other yolk-shell nanostructures (e.g. FePt@Fe_2O_3 (119) and Pt@CoO (120)) are successfully synthesized by the same Kirkendall effect mechanism on the shell of core-shell intermediates. Yolk-shell nanoboxes of monodispersed metal sulfide of Ag_2S, CdS, PbS, ZnS, and $AgInS_2$ with sizes of ≈220 nm were synthesized through a self-sacrificing template route with two steps of ion-exchange based on the Kirkendall effect (121). In the synthesis procedure, a Na_2S solution was injected into the prepared AgCl suspension and the obtained Ag2S was employed to synthesize the other metal sulfides. Typically, Ag_2S was redispersed in methanol $Cd(NO_3)_2$ and then methanolic solution containing PVP was added and heated to 50 °C. Finally, a certain amount of TBP was added to the mixture and maintained under stirring at 50 (C for 2 h. emplate-free hydrothermal route was developed to synthesize Pt@CeO_2 nanocomposite with tunable core-shell and yolk-shell structures (122). Multifunctional Ag@Fe_2O_3 yolk-shell nanoparticles were synthesized by the Kirkendall effect, and applied for simultaneous capture, killing, and removal of pathogens. After the surface functionalization by glucose, the Ag@Fe_2O_3-glucose conjugates showed both high capture efficiency of bacteria

and potent antibacterial activity (123).

4. CONCLUSION

In the Kirkendall effect, different atoms can migrate with different rates, leading to a shift in the diffusion interface. The Kirkendall effect can also act as sacrificial template. This templating method is essentially advantageous because it needs no extra surface functionalization and shell fabrication. For instance, the control of the size of interior nanopores is possible by means of annealing in high temperatures. Hence, the advantage of using this physical phenomenon is in the generation of all kinds of hollow nanoobjects. Furthermore, estimation of thermodynamics and kinetic aspects indicated that a hollow nanosize particle is thermodynamically unstable. Nanostructure materials synthesized via the Kirkendall effect represent useful properties, such as biocompatibility, magnetism, excellent bioconjugation ability, plasmon resonance and in vivo targeting efficiency that make them promising candidates for use in bioassay, sensing, drug delivery system, bioimaging, photothermal therapy, magnetic hyperthermia, and simultaneous diagnosis and therapy.

ACKNOWLEDGMENT

We would like to thank the Research Council of Shiraz University of Medical Sciences (12340) for supporting this research.

FUNDING/SUPPORT

Not mentioned any Funding/Support by authors.

AUTHORS CONTRIBUTION

This work was carried out in collaboration among all authors.

CONFLICT OF INTEREST

The authors declared no potential conflicts of interests with respect to the authorship and/or publication of this paper.

REFERENCES

1. Nakajima H. The discovery and acceptance of the Kirkendall effect: The result of a short research career. JOM. 1997;49(6):15-9.
2. Fan HJ, Gösele U, Zacharias M. Formation of nanotubes and hollow nanoparticles based on Kirkendall and diffusion processes: a review. small. 2007;3(10):1660-71.
3. Narasimhan T. Energetics of the Kirkendall effect. Current Science. 2007;93(9):1257-64.
4. An K, Hyeon T. Synthesis and biomedical applications of hollow nanostructures. Nano Today. 2009;4(4):359-73.
5. Fan HJ, Knez M, Scholz R, Hesse D, Nielsch K, Zacharias M, et al. Influence of surface diffusion on the formation of hollow nanostructures induced by the Kirkendall effect: the basic concept. Nano letters. 2007;7(4):993-7.
6. Wang W, Dahl M, Yin Y. Hollow nanocrystals through the nanoscale Kirkendall effect. Chemistry of Materials. 2012;25(8):1179-89.
7. Chiang R-K, Chiang R-T. Formation of hollow Ni2P nanoparticles based on the nanoscale Kirkendall effect. Inorganic chemistry. 2007;46(2):369-71.
8. Liu J, Xue D. Thermal oxidation strategy towards porous metal oxide hollow architectures. Advanced Materials. 2008;20(13):2622-7.
9. Huang CC, Hwu JR, Su WC, Shieh DB, Tzeng Y, Yeh CS. Surfactant-Assisted Hollowing of Cu Nanoparticles Involving Halide-Induced Corrosion–Oxidation Processes. Chemistry–A European Journal. 2006;12(14):3805-10.
10. Kim MR, Jang D-J. One-step fabrication of well-defined hollow CdS nanoboxes. Chemical Communications. 2008 (41):5218-20.
11. Xu H, Wang W. Template synthesis of multishelled Cu2O hollow spheres with a single-crystalline shell wall. Angewandte Chemie International Edition. 2007;46(9):1489-92.
12. Bao J-c, Liang Y-y, Xu Z, Si L. Facile synthesis of hollow nickel submicrometer spheres. Advanced Materials. 2003;15(21):1832-5.
13. Skrabalak SE, Chen J, Sun Y, Lu X, Au L, Cobley CM, et al. Gold nanocages: synthesis, properties, and applications. Accounts of Chemical Research. 2008;41(12):1587-95.
14. Chen J, Saeki F, Wiley BJ, Cang H, Cobb MJ, Li Z-Y, et al. Gold nanocages: bioconjugation and their potential use as optical imaging contrast agents. Nano letters. 2005;5(3):473-7.
15. Lou XWD, Archer LA, Yang Z. Hollow micro-/nanostructures: Synthesis and applications. Advanced Materials. 2008;20(21):3987-4019.
16. Knez M, Scholz R, Nielsch K, Pippel E, Hesse D, Zacharias M, et al. Monocrystalline spinel nanotube fabrication based on the Kirkendall effect. Nature materials. 2006;5(8):627-31.
17. Van der Ven A, Yu H-C, Ceder G, Thornton K. Vacancy mediated substitutional diffusion in binary crystalline solids. Progress in Materials Science. 2010;55(2):61-105.
18. Tu K, Gösele U. Hollow nanostructures based on the Kirkendall effect: design and stability considerations. Applied Physics Letters. 2005;86(9):093111.
19. Nakamura R, Nakajima H, editors. Structural stability of hollow oxide nanoparticles at high temperatures. Journal of Physics: Conference Series; 2009: IOP Publishing.
20. Peng S, Sun S. Synthesis and characterization of monodisperse hollow Fe3O4 nanoparticles. Angewandte Chemie. 2007;119(22):4233-6.
21. Blomberg S, Ostberg S, Harth E, Bosman AW, Van Horn B, Hawker CJ. Production of crosslinked, hollow nanoparticles by surface-initiated living free-radical polymerization. Journal of Polymer Science Part A: Polymer Chemistry. 2002;40(9):1309-20.
22. Cheng K, Sun S. Recent advances in syntheses and therapeutic applications of multifunctional porous hollow nanoparticles. Nano Today. 2010;5(3):183-96.
23. Niu K-Y, Park J, Zheng H, Alivisatos AP. Revealing bismuth oxide hollow nanoparticle formation by the Kirkendall effect. Nano letters. 2013;13(11):5715-9.
24. Ha D-H, Moreau LM, Honrao S, Hennig RG, Robinson RD. The oxidation of cobalt nanoparticles into Kirkendall-hollowed CoO and Co3O4: The diffusion mechanisms and atomic structural transformations. The Journal of Physical Chemistry C. 2013;117(27):14303-12.
25. Zhou J, Ma L, Song H, Wu B, Chen X. Durable high-rate performance of CuO hollow nanoparticles/graphene-nanosheet composite anode material for lithium-ion batteries. Electrochemistry Communications. 2011;13(12):1357-60.
26. Kong M, Zhang W, Yang Z, Weng S, Chen Z. Facile synthesis of CuO hollow nanospheres assembled by nanoparticles and their electrochemical performance. Applied Surface Science. 2011;258(4):1317-21.
27. Nakamura R, Tokozakura D, Nakajima H, Lee J-G, Mori H. Hollow oxide formation by oxidation of Al and Cu nanoparticles. Journal of applied physics. 2007;101(7):074303.
28. Niu K, Yang J, Kulinich S, Sun J, Du X. Hollow nanoparticles of metal oxides and sulfides: fast preparation via laser ablation in liquid. Langmuir. 2010;26(22):16652-7.
29. Jaffari GH, Ceylan A, Ni C, Shah SI. Enhancement of surface spin disorder in hollow NiFe2O4 nanoparticles. Journal of Applied Physics. 2010;107(1):013910.
30. Kamdem DP, Bose SK, Luner P. Inverse gas chromatography characterization of birch wood meal. Langmuir. 1993;9(11):3039-44.
31. Chen L, Dai H, Shen Y, Bai J. Size-controlled synthesis and magnetic properties of NiFe 2 O 4 hollow nanospheres via a gel-assistant hydrothermal route. Journal of Alloys and Compounds. 2010;491(1):L33-L8.
32. Zheng X, Yuan S, Tian Z, Yin S, He J, Liu K, et al. One-pot synthesis of hollow nickel phosphide nanoparticles with tunable void sizes using triphenylphosphine. Materials Letters. 2009;63(27):2283-5.
33. Wang J, Johnston-Peck AC, Tracy JB. Nickel phosphide nanoparticles with hollow, solid, and amorphous structures. Chemistry of Materials. 2009;21(19):4462-7.
34. Chen G, Niu M, Cui L, Bao F, Zhou L, Wang Y. Facile synthesis and formation mechanism of metal chalcogenides hollow nanoparticles. The Journal of Physical Chemistry C. 2009;113(18):7522-5.
35. Jana S, Chang JW, Rioux RM. Synthesis and modeling of hollow intermetallic Ni–Zn nanoparticles formed by the Kirkendall effect. Nano letters. 2013;13(8):3618-25.
36. Sun H, Chen Y, Wang X, Xie Y, Li W, Zhang X. Synthesis of ZnS hollow nanoneedles via the nanoscale Kirkendall effect. Journal of Nanoparticle Research. 2011;13(1):97-103.
37. Cantane D, Oliveira F, Santos S, Lima F. Synthesis of Pt-based hollow nanoparticles using carbon-supported Co@ Pt and Ni@ Pt core–shell structures as templates: electrocatalytic activity for the oxygen reduction reaction. Applied Catalysis B: Environmental. 2013;136:351-60.
38. Gullapalli S, Grider JM, Bagaria HG, Lee K-S, Cho M, Colvin VL, et al. Molten-droplet synthesis of composite CdSe hollow nanoparticles. Nanotechnology. 2012;23(49):495605.
39. Wu Y, Yu H, Peng F, Wang H. Facile synthesis of porous hollow iron oxide nanoparticles supported on carbon nanotubes. Materials Letters. 2012;67(1):245-7.
40. Ben Moshe A, Markovich G. Synthesis of single crystal hollow silver nanoparticles in a fast reaction-diffusion process. Chemistry of Materials. 2011;23(5):1239-45.

41. Zhou J, Song H, Chen X, Zhi L, Huo J, Cheng B. Oxidation conversion of carbon-encapsulated metal nanoparticles to hollow nanoparticles. Chemistry of Materials. 2009;21(15):3730-7.
42. Hungerford G, Allison A, McLoskey D, Kuimova MK, Yahioglu G, Suhling K. Monitoring sol-to-gel transitions via fluorescence lifetime determination using viscosity sensitive fluorescent probes. The Journal of Physical Chemistry B. 2009;113(35):12067-74.
43. Lei X, Yaoqi L, Rong Y, Yang L, Xingguo L. Superior hydrogen desorption kinetics of Mg (NH {sub 2})\{sub 2} hollow nanospheres mixed with MgH {sub 2} nanoparticles. Applied Physics Letters. 2008;92(23).
44. Zolotaryov A, Goetze S, Zierold R, Novikov D, Birajdar B, Hesse D, et al. Temperature-Dependent Solid-State Reactions With and Without Kirkendall Effect in Al2O3/ZnO, Fe2O3/ZnO, and CoXOY/ZnO Oxide Thin Film Systems. Advanced Engineering Materials. 2010;12(6):509-16.
45. Mimani T. Instant synthesis of nanoscale spinel aluminates. Journal of alloys and compounds. 2001;315(1):123-8.
46. Knez M, Nielsch K, Niinistö L. Synthesis and surface engineering of complex nanostructures by atomic layer deposition. Advanced Materials. 2007;19(21):3425-38.
47. Rao C, Vivekchand S, Biswas K, Govindaraj A. Synthesis of inorganic nanomaterials. Dalton Transactions. 2007 (34):3728-49.
48. Yang Y, Kim DS, Knez M, Scholz R, Berger A, Pippel E, et al. Influence of temperature on evolution of coaxial ZnO/Al2O3 one-dimensional heterostructures: From core-shell nanowires to spinel nanotubes and porous nanowires. The Journal of Physical Chemistry C. 2008;112(11):4068-74.
49. Fan H, Knez M, Scholz R, Nielsch K, Pippel E, Hesse D, et al. Single-crystalline MgAl2O4 spinel nanotubes using a reactive and removable MgO nanowire template. Nanotechnology. 2006;17(20):5157.
50. Ahn H, Lee J. Effects of a low-temperature sulfidation process on the microstructural properties of ZnO nanowires: ZnS formation and nanoscale Kirkendall effect. CrystEngComm. 2013;15(34):6709-14.
51. Wang Z, Pan L, Hu H, Zhao S. Co 9 S 8 nanotubes synthesized on the basis of nanoscale Kirkendall effect and their magnetic and electrochemical properties. CrystEngComm. 2010;12(6):1899-904.
52. Kong J, Wong SY, Zhang Y, Tan HR, Li X, Lu X. One-dimensional carbon–SnO 2 and SnO 2 nanostructures via single-spinneret electrospinning: tunable morphology and the underlying mechanism. Journal of Materials Chemistry. 2011;21(40):15928-34.
53. Kong J, Tan HR, Tan SY, Li F, Wong SY, Li X, et al. A generic approach for preparing core–shell carbon–metal oxide nanofibers: morphological evolution and its mechanism. Chemical Communications. 2010;46(46):8773-5.
54. İpeksaç T, Kaya F, Kaya C. Hydrothermal synthesis of Zinc oxide (ZnO) nanotubes and its electrophoretic deposition on nickel filter. Materials Letters. 2013;100:11-4.
55. Ma P, Jie Y, Jin GY, Xu XL, Ren ZY, Fan HM. Formation of thin tubular ZnO nanostructure through spontaneously formed porous Zn/ZnO nanoparticles. IET Micro & Nano Letters. 2013;8(5):267-70.
56. Shi L, Dai Y. Synthesis and photocatalytic activity of Zn 2 SnO 4 nanotube arrays. Journal of Materials Chemistry A. 2013;1(41):12981-6.
57. Chen Y-C, Chen K-B, Lee C-S, Lin M. Direct synthesis of Zr-doped ceria nanotubes. The Journal of Physical Chemistry C. 2009;113(13):5031-4.
58. Ding R, Liu J, Jiang J, Li Y, Hu Y, Ji X, et al. High surface area ZnO–carbon composite tubular arrays based on the Kirkendall effect and in situ Zn evaporation. Chemical Communications. 2009 (30):4548-50.
59. Jitputti J, Charoensirithavorn P, Yoshikawa S. Hydrothermal production of SrTiO3 nanotube arrays. Chemistry letters. 2007;36(12):1508-9.
60. Chen X, Zhang Z, Qiu Z, Shi C, Li X. Hydrothermal fabrication and characterization of polycrystalline linneite (Co 3 S 4) nanotubes based on the Kirkendall effect. Journal of colloid and interface science. 2007;308(1):271-5.
61. Ding S, Xu C, Wang W, Huang Y, Zhen L. Formation of tubular BaTiO 3 nanoparticle assembly through the Kirkendall effect using Na 2 Ti 3 O 7 nanowires as template. Materials Research Bulletin. 2013;48(11):4565-9.
62. Liao M-Y, Huang C-C, Chang M-C, Lin S-F, Liu T-Y, Su C-H, et al. Synthesis of magnetic hollow nanotubes based on the kirkendall effect for MR contrast agent and colorimetric hydrogen peroxide sensor. Journal of Materials Chemistry. 2011;21(22):7974-81.
63. Lv Y, Li Y, Shen W. Synthesis of Co 3 O 4 nanotubes and their catalytic applications in CO oxidation. catalysis communications. 2013;42:116-20.
64. Song X, Gao L, Mathur S. Synthesis, characterization, and gas sensing properties of porous nickel oxide nanotubes. The Journal of Physical Chemistry C. 2011;115(44):21730-5.
65. Qiu Y, Yang S. Kirkendall approach to the fabrication of ultra-thin ZnO nanotubes with high resistive sensitivity to humidity. Nanotechnology. 2008;19(26):265606.
66. Raidongia K, Rao C. Study of the transformations of elemental nanowires to nanotubes of metal oxides and chalcogenides through the Kirkendall effect. The Journal of Physical Chemistry C. 2008;112(35):13366-71.
67. Lee Y-I, Goo Y-S, Chang C-H, Lee K-J, Myung NV, Choa Y-H. Tunable synthesis of cuprous and cupric oxide nanotubes from electrodeposited copper nanowires. Journal of nanoscience and nanotechnology. 2011;11(2):1455-8.
68. Ren Y, Chim WK, Chiam SY, Huang JQ, Pi C, Pan JS. Formation of Nickel Oxide Nanotubes with Uniform Wall Thickness by Low-Temperature Thermal Oxidation Through Understanding the Limiting Effect of Vacancy Diffusion and the Kirkendall Phenomenon. Advanced Functional Materials. 2010;20(19):3336-42.
69. Lai M, Mubeen S, Chartuprayoon N, Mulchandani A, Deshusses MA, Myung NV. Synthesis of Sn doped CuO nanotubes from core? shell Cu/SnO2 nanowires by the Kirkendall effect. Nanotechnology. 2010;21(29):295601.
70. Zhang G, Yu Q, Yao Z, Li X. Large scale highly crystalline Bi2Te3 nanotubes through solution phase nanoscale Kirkendall effect fabrication. Chemical Communications. 2009 (17):2317-9.
71. Shao H, Qian X, Huang B. Fabrication of single-crystal ZnO nanorods and ZnS nanotubes through a simple ultrasonic chemical solution method. Materials Letters. 2007;61(17):3639-43.
72. Li W, Tao M, SHENG W, Xuefeng G, Weiping D, Yi C. Preparation, characterization, and properties of ferric molybdate nanotubes for propene epoxidation by air. Chinese Journal of Catalysis. 2009;30(8):711-3.
73. Wang L, Peng B, Guo X, Ding W, Chen Y. Ferric molybdate nanotubes synthesized based on the Kirkendall effect and their catalytic property for propene epoxidation by air. Chemical Communications. 2009 (12):1565-7.
74. Lu HB, Liao L, Li H, Wang DF, Tian Y, Li JC, et al. Hollow MgO nanotube arrays by using ZnO nanorods as templates. European Journal of Inorganic Chemistry. 2008;2008(17):2727-32.
75. Wang Q, Li J-X, Li G-D, Cao X-J, Wang K-J, Chen J-S. Formation of CuS nanotube arrays from CuCl Nanorods through a gas-solid reaction route. Journal of crystal growth. 2007;299(2):386-92.
76. Chen G, Sun S, Sun X, Fan W, You T. Formation of CeO2 nanotubes from Ce (OH) CO3 nanorods through kirkendall diffusion. Inorganic chemistry. 2009;48(4):1334-8.
77. Kumarakuru H, Cherns D. The preferential growth of ZnS on ZnOnanorods. Journal of Solid State Chemistry. 2013;199:109-15.
78. Fu J, Zhang J, Peng Y, Zhao C, He Y, Zhang Z, et al. Wire-in-tube structure fabricated by single capillary electrospinning via nanoscale Kirkendall effect: the case of nickel–zinc ferrite. Nanoscale. 2013;5(24):12551-7.
79. Wan H, Jiang J, Yu J, Xu K, Miao L, Zhang L, et al. NiCo 2 S 4 porous nanotubes synthesis via sacrificial templates: high-performance electrode materials of supercapacitors. CrystEngComm. 2013;15(38):7649-51.
80. Lu Y, Tu J, Xiong Q, Qiao Y, Zhang J, Gu C, et al. Carbon-Decorated Single-Crystalline Ni2P Nanotubes Derived from Ni Nanowire Templates: A High-Performance Material for Li-Ion Batteries. Chemistry–A European Journal. 2012;18(19):6031-8.
81. Jiang Z, Zhang Q, Zong C, Liu B-J, Ren B, Xie Z, et al. Cu–Au alloy nanotubes with five-fold twinned structure and their application in surface-enhanced Raman scattering. Journal of Materials Chemistry. 2012;22(35):18192-7.
82. Xu J, Tang Y-B, Zhang W, Lee C-S, Yang Z, Lee S-T. Fabrication of architectures with dual hollow structures: Arrays of Cu2O nanotubes organized by hollow nanospheres. Crystal Growth & Design. 2009;9(10):4524-8.
83. Wang Q, Chen G, Wang L, Zhou C, Xu S. Self-sacrificed template method for the synthesis of ZnO-tubular nanostructures: reaction kinetics and pathways. Journal of Crystal Growth. 2009;311(16):3978-83.
84. Mondragon-Galicia G, Perez-Hernandez R, Gutierrez-Wing C, Mendoza-Anaya D. A novel synthesis method to produce silver-doped CeO2 nanotubes based on Ag nanowire templates. Physical Chemistry Chemical Physics. 2011;13(37):16756-61.
85. Peng Q, Sun X-Y, Spagnola JC, Saquing C, Khan SA, Spontak RJ, et al. Bi-directional Kirkendall effect in coaxial microtube nanolaminate assemblies fabricated by atomic layer deposition. ACS nano. 2009;3(3):546-54.
86. Sreeprasad T, Pradeep T. Tubular nanostructures of Cr2Te4O11 and Mn2TeO6 through room-temperature chemical transformations of tellurium nanowires. The Journal of Physical Chemistry C. 2011;115(33):16524-36.
87. Shuai X, Shen W. A facile chemical conversion synthesis of ZnO/ZnS core/shell nanorods and diverse metal sulfide nanotubes. The Journal of Physical Chemistry C. 2011;115(14):6415-22.
88. Cummins DR, Russell HB, Jasinski JB, Menon M, Sunkara MK. Iron sulfide (FeS) nanotubes using sulfurization of hematite nanowires. Nano letters. 2013;13(6):2423-30.
89. Han J, Wang L, Guo R. Facile synthesis of hierarchical conducting polymer nanotubes derived from nanofibers and their application for controlled drug release. Macromolecular rapid communications. 2011;32(9-10):729-35.
90. Li C, Bando Y, Dierre B, Sekiguchi T, Huang Y, Lin J, et al. Effect of Size-Dependent Thermal Instability on Synthesis of Zn 2 SiO 4-SiO x Core–Shell Nanotube Arrays and Their Cathodoluminescence Properties. Nanoscale research letters. 2010;5(4):773.
91. Wang Q, Geng B, Wang S, Ye Y, Tao B. Modified Kirkendall effect for fabrication of magnetic nanotubes. Chemical Communications. 2010;46(11):1899-901.
92. Zeng J, Liu C, Huang J, Wang X, Zhang S, Li G, et al. UV-light induced fabrication of CdCl2 nanotubes through CdSe/Te nanocrystals based on dimension and configuration control. Nano letters. 2008;8(5):1318-22.
93. Cai K, Lv Z, Chen K, Huang L, Wang J, Shao F, et al. Aqueous synthesis of porous platinum nanotubes at room temperature and their intrinsic peroxidase-like activity. Chemical Communications. 2013;49(54):6024-6.
94. Liu F, Xue D. Fabrication of Branched Nanotubes of Sodium Niobate. Surface Review and Letters. 2010;17(03):363-7.
95. El Mel A-A, Buffière M, Tessier P-Y, Xu W, Du K, Choi C-H, et al., editors. Fabrication of highly ordered hollow oxide nanostructures based on nanoscale Kirkendall effect and Ostwald ripening. Nanoelectronics Conference (INEC), 2013 IEEE 5th International; 2013: IEEE.
96. Ibáñez M, Fan J, Li W, Cadavid D, Nafria R, Carrete A, et al. Means and limits of control of the shell parameters in hollow nanoparticles obtained by the Kirkendall effect. Chemistry of Materials. 2011;23(12):3095-104.
97. Liu L, Yoo S-H, Park S. Synthesis of vertically aligned hollow platinum nanotubes with single crystalline nanoflakes. Chemistry of Materials. 2010;22(8):2681-4.
98. Fang X, Gautam UK, Bando Y, Dierre B, Sekiguchi T, Golberg D. Multiangular branched ZnS nanostructures with needle-shaped tips: potential luminescent and field-emitter nanomaterial. The Journal of Physical Chemistry C. 2008;112(12):4735-42.
99. Boo H, Jeong R-A, Park S, Kim KS, An KH, Lee YH, et al. Electrochemical nanoneedle biosensor based on multiwall carbon nanotube. Analytical chemistry. 2006;78(2):617-20.

100. Lee W, Jeong M-C, Kim MJ, Myoung J-M. Field emission characteristics of ZnO nanoneedle array cell under ultraviolet irradiation. Physics Letters A. 2007;370(3):345-50.
101. Cao B, Cai W, Duan G, Li Y, Zhao Q, Yu D. A template-free electrochemical deposition route to ZnO nanoneedle arrays and their optical and field emission properties. Nanotechnology. 2005;16(11):2567.
102. Oh B, Lee CH. Nanofiber for cardiovascular tissue engineering. Expert opinion on drug delivery. 2013;10(11):1565-82.
103. Nguyen LT, Chen S, Elumalai NK, Prabhakaran MP, Zong Y, Vijila C, et al. Biological, chemical, and electronic applications of nanofibers. Macromolecular materials and engineering. 2013;298(8):822-67.
104. Matlock-Colangelo L, Baeumner AJ. Recent progress in the design of nanofiber-based biosensing devices. Lab on a Chip. 2012;12(15):2612-20.
105. Xia X, Dong X, Wei Q, Cai Y, Lu K. Formation mechanism of porous hollow SnO2 nanofibers prepared by one-step electrospinning. Express Polym Lett. 2012;6:169-76.
106. Subbiah T, Bhat G, Tock R, Parameswaran S, Ramkumar S. Electrospinning of nanofibers. Journal of Applied Polymer Science. 2005;96(2):557-69.
107. Frenot A, Chronakis IS. Polymer nanofibers assembled by electrospinning. Current opinion in colloid & interface science. 2003;8(1):64-75.
108. Liu P, Zhu Y, Ma J, Yang S, Gong J, Xu J. Preparation of continuous porous alumina nanofibers with hollow structure by single capillary electrospinning. Colloids and Surfaces A: Physicochemical and Engineering Aspects. 2013;436:489-94.
109. Jain M, Jia Q, Kozuka H, Goh GK. Program-Symposium M: Solution Synthesis of Inorganic Functional Materials—Films, Nanoparticles, and Nanocomposites.
110. Liang X, Wang X, Zhuang Y, Xu B, Kuang S, Li Y. Formation of CeO2-ZrO2 solid solution nanocages with controllable structures via Kirkendall effect. Journal of the American Chemical Society. 2008;130(9):2736-7.
111. Wang J, Xu W, Chen L, Jia Y, Wang L, Huang X-J, et al. Excellent fluoride removal performance by CeO 2–ZrO 2 nanocages in water environment. Chemical engineering journal. 2013;231:198-205.
112. Sun S, Deng D, Song X, Yang Z. Elucidating a twin-dependent chemical activity of hierarchical copper sulfide nanocages. Physical Chemistry Chemical Physics. 2013;15(38):15964-70.
113. Kuo CH, Chu YT, Song YF, Huang MH. Cu2O Nanocrystal-Templated Growth of Cu2S Nanocages with Encapsulated Au Nanoparticles and In-Situ Transmission X-ray Microscopy Study. Advanced Functional Materials. 2011;21(4):792-7.
114. Hu L, Yan N, Chen Q, Zhang P, Zhong H, Zheng X, et al. Fabrication based on the kirkendall effect of Co3O4 porous nanocages with extraordinarily high capacity for lithium storage. Chemistry–A European Journal. 2012;18(29):8971-7.
115. Cao H, Qian X, Zai J, Yin J, Zhu Z. Conversion of Cu 2 O nanocrystals into hollow Cu 2− x Se nanocages with the preservation of morphologies. Chemical communications. 2006 (43):4548-50.
116. Liu J, Qiao SZ, Chen JS, Lou XWD, Xing X, Lu GQM. Yolk/shell nanoparticles: new platforms for nanoreactors, drug delivery and lithium-ion batteries. Chemical Communications. 2011;47(47):12578-91.
117. Zhao Y, Jiang L. Hollow micro/nanomaterials with multilevel interior structures. Advanced Materials. 2009;21(36):3621-38.
118. Gao J, Liang G, Zhang B, Kuang Y, Zhang X, Xu B. FePt@ CoS2 yolk-shell nanocrystals as a potent agent to kill HeLa cells. Journal of the American Chemical Society. 2007;129(5):1428-33.
119. Gao J, Liang G, Cheung JS, Pan Y, Kuang Y, Zhao F, et al. Multifunctional yolk− shell nanoparticles: A potential MRI contrast and anticancer agent. Journal of the American Chemical Society. 2008;130(35):11828-33.
120. Park JC, Song H. Metal@ silica yolk-shell nanostructures as versatile bifunctional nanocatalysts. Nano Research. 2011;4(1):33-49.
121. Qin Z, Sun H, Jiang Z, Jiao X, Chen D. Synthesis of metal sulfide nanoboxes based on Kirkendall effect and Pearson hardness. CrystEngComm. 2013;15(5):897-902.
122. Zhang N, Fu X, Xu Y-J. A facile and green approach to synthesize Pt@ CeO 2 nanocomposite with tunable core-shell and yolk-shell structure and its application as a visible light photocatalyst. Journal of Materials Chemistry. 2011;21(22):8152-8.
123. Wei Z, Zhou Z, Yang M, Lin C, Zhao Z, Huang D, et al. Multifunctional Ag@ Fe 2 O 3 yolk–shell nanoparticles for simultaneous capture, kill, and removal of pathogen. Journal of Materials Chemistry. 2011;21(41):16344-8.